Observation of energetic-ion losses induced by various MHD instabilities in the Large Helical Device (LHD)

Observation of Energetic-Ion Losses Induced by Various MHD Instabilities

in the Large Helical Device (LHD)

K. Ogawa[1], M. Isobe, K. Toi, F. Watanabe[2], D. A.Spong[3], A. Shimizu, M. Osakabe,

S. Ohdachi, S. Sakakibara, and LHD Experiment Group

National Institute for Fusion Science, 322-6 Oroshi-cho, Toki 509-5292, Japan

[1]Department of Energy Science and Engineering, Nagoya University, Nagoya 464-8603, Japan

[2]Graduate School of Energy Science, Kyoto University, Kyoto 606-8502, Japan

[3]Oak Ridge National Laboratory, Oak Ridge, Tennessee 37831-6169, USA

email:ogawa.kunihiro@lhd.nifs.ac.jp

Abstract

Energetic-ion losses induced by toroidicity-induced Alfvén eigenmodes (TAEs) and resistive

interchange modes (RICs) were observed in neutral-beam heated plasmas of the Large Helical

Device (LHD) at a relatively low toroidal magnetic field level (≤ 0.75 T). The energy and pitch

angle of lost ions are detected using a scintillator-based lost-fast ion probe. Each instability

increases the lost ions having certain energy/pitch angle. TAE bursts preferentially induce

energetic beam ions in co-passing orbits having energy from the injection energy E=190keV down to 130keV, while RICs expel energetic ions of E=190 keV down to ~130keV in passing-toroidally trapped boundary orbits. Loss fluxes induced by these instabilities increase with different dependencies on the magnetic fluctuation amplitude: nonlinear and linear dependencies for TAEs and RICs, respectively.

1. Introduction

The self-sustained D-T burning plasma can be realized under the condition that fusion-born energetic alpha particles (α's) are confined long enough to heat the bulk plasma [1]. In addition to effective alpha heating of bulk plasma, loss of α's should be suppressed down to an acceptable level to prevent plasma-facing components from the localized damage due to the impact of escaping α's. Better understanding of transport and loss process of these energetic ions is therefore essentially required to realize a nuclear fusion reactor. The principal concern is that D-T produced α's and super-Alfvénic ions produced by neutral beam (NB) injection or ion cyclotron resonance heating may destabilize energetic-ion-driven magnetohydrodynamic (MHD) instabilities such as Alfvén eigenmodes (AEs) [2] and energetic-particle-continuum modes (EPMs) [3] because those instabilities can potentially cause radial transport and/or losses of energetic ions through wave-particle resonance processes. Effect of MHD instabilities driven

by the bulk plasma, such as sawtooth and tearing mode (TM) on energetic ion transport is also

of great concern since transport of energetic ion may be affected through not only wave-particle

resonance but also stochastization of energetic-ion orbits [4].

Energetic-ion losses induced by AEs have been so far studied experimentally in

several tokamaks [5-7]. Previously, detailed loss processes of energetic ions due to AEs were

studied in TFTR and JT60-U [7-9]. In TFTR, a scintillator-based lost fast ion probe (SLIP) was

employed to simultaneously measure the energy E and pitch angle χ of escaping fusion products

and beam ions [10, 11]. In those experiments, decreases of neutron emission rate, and at the

same time, increase of energetic-ion losses due to global Alfvén eigenmodes (GAEs) were

observed [7]. Nowadays, efforts on numerical simulations are being made to reveal the

energetic-ion transport due to energetic-ion-driven MHD instabilities [12, 13]. In addition,

MHD instabilities driven by the bulk plasma can potentially induce redistribution and/or losses

of energetic ions. It has been experimentally observed that significant redistribution of energetic

ions is caused by sawteeth in tokamaks [14-16]. Also, it has been recognized that a TM leads to

redistribution and/or loss of energetic ions. Reduction of the NB current drive efficiency caused

by beam-ion losses due to TMs was observed in DIII-D [17] and also energetic-ion loss by

neoclassical TM was recently discussed in ASDEX-U [18]. In both cases, beam-ion losses are

interpreted to be due to stochastization of beam-ion orbits. At present, energetic-ion losses due

not only to energetic-ion-driven MHD modes but also pressure/current-driven MHD modes are intensively studied using the SLIP in NSTX, ASDEX-U and JET [19-21].

It is also of importance for helical/stellarator plasmas to understand anomalous radial transport and/or loss of energetic ions caused by various MHD instabilities. In experiments prior to this work, anomalous beam-ion losses induced by toroidicity-induced Alfvén eigenmodes (TAEs) and EPMs were measured with the SLIP on medium-scale stellarators/helical devices, i.e. CHS[22, 23] and W7-AS [24]. In this paper, we present characteristics of beam-ion losses due to both MHD instabilities, i.e. energetic-ion driven TAEs and pressure-driven resistive-interchange (RIC) modes [25] in high β discharges with $\upsilon_b > \upsilon_A$ beam (υ_b and υ_A indicate the velocity of beam and Alfvén speed) of a large-scale helical device where energetic ions are well confined, compared with these medium-sized devices. Beam-ion losses are studied by use of the SLIP, which has recently been installed at the outboard side of the Large Helical Device (LHD) to investigate behaviours of co-going beam ions [26-28].

This paper is organized as follows. In Sec. 2, the brief descriptive introduction of LHD and the SLIP is presented. Characteristics of TAE-induced beam ion loss, i.e. energy and pitch angles of escaping beam ions due to TAE burst, and high-frequency fluctuations seen on energetic-ion loss signals are presented in Sec. 3. Anomalous losses of energetic-ions induced by RIC mode are also reported in Sec. 3. Sec. 4 gives a summary. Finally, the equations to

calculate Hα fluctuations induced by TAE mode are given in Appendix 1. The dispersion

relation of RIC is also given in Appendix 2.

2. Experimental Setups

LHD is a large helical device having number of toroidal periods M of 10 and

multipolarity l of 2. The major radius R_0 and plasma minor radius a are 3.9 m and ~ 0.6 m,

respectively. LHD is equipped with three negative-ion-source based NB injectors of which

injection energy E_b is up to 190 keV. One of three tangentially injects NBs in the opposite

direction of the equivalent-plasma current whereas the others tangentially inject NBs in the

direction of the equivalent-plasma current in counter clockwise B_t which is defined from the top

view of the torus. Injected beam ions are super-Alfvénic in many cases and often destabilize

TAEs [29, 30].

The SLIP important in this work has been lately developed and installed at the

outboard side of the LHD torus. It is actually a magnetic spectrometer using a set of apertures

and a scintillator plate (ZnS:Ag), providing energy E and pitch angles $\chi=\arccos(v_{//}/v)$ of lost

energetic ions simultaneously as a function of time, where $v_{//}$ is velocity of ion parallel to

magnetic field and v is velocity of ion. The detailed description of the design concept and

hardware of SLIP on LHD are available in Ref. 26. Figure 1a shows the installation position of

SLIP and typical orbit of co-going energetic ion reaching the SLIP. Figure 1b shows the relation

between the pitch angle at the plasma surface and that of at the SLIP position. As seen from

Fig.1b, the differences of χ between the SLIP position and that at the plasma surface from which

position the energetic ion is lost to the SLIP are in the range of ±10 degrees.

Luminous image produced on the scintillator screen is transferred to the outside of

vacuum vessel and subsequently is divided by a half mirror into two paths. Each scintillation

light image is monitored with a 4×4-photomultiplier tube (PMT) array and a CMOS camera,

simultaneously. Relative sensitivity of PMTs is calibrated with an electro-luminescence sheet

emitting a blue-green light uniformly within 10 % error. The detection ranges of gyroradius

centroid $\rho_h = \dfrac{\sqrt{2Em_h}}{qB_{SLIP}}$ and χ of lost-energetic ions on the scintillator screen of the SLIP

are shown in Fig. 2 for the vacuum magnetic configuration of the magnetic axis position R_{ax} of

3.6 m. Here, m_h, q and B_{SLIP} represent for the ion mass, elementary electronic charge and the

magnetic field strength at the SLIP head position, respectively. Ranges of the detectable ρ_h and

χ are ~ 2 cm to 23 cm and ~ 25 deg. to 75 deg., respectively, where ρ_h ~ 17.0 cm correspond

to E ~ 190 keV at the field strength B_t=0.6 T on the magnetic axis, that is, B_{SLIP}=0.37T. E and χ

shown in this paper stand for those at the SLIP position. The PMT array having high-time

resolution up to 2 μs is used to detect rapid events related to TAE and EPM. The camera system

is slow in time response but can provide detailed information of E and χ with a 353×353

pixels image. The typical frame rate is 500 frames/s.

In addition to the above-mentioned SLIP, the E//B-type neutral-particle analyser (NPA) having a tangential line of sight was employed to detect fast neutrals charge-exchanged with co-going energetic ions [31]. Magnetic fluctuations were detected using toroidal/poloidal magnetic probe (MP) arrays placed on the vacuum vessel. Toroidal/poloidal MP arrays consist of 6/13 MPs and are used for analysis of toroidal/poloidal mode numbers of magnetic fluctuations [32]. Information of radial structure of AEs was obtained with a fast-response Hα array system (FHA), of which system consists of interference filters (transmission wavelength is from 654 nm to 658 nm) and seven PMTs characterized by fast-time response up to 200 kHz [33]. The sight line of FHA is shown in Fig.1c. Note that the FHA is applicable to any ranges of density and magnetic field strength without rigorous limitations in these parameters like electron cyclotron emission diagnostic. Radial structure of RIC was derived with several soft-x ray arrays (SX) or absolute-extreme ultraviolet (AXUV) arrays [34], where each array consists of 20 SX/AXUV detectors (Fig. 1d).

3. Experimental results

3.1 Typical discharges with toroidal Alfvén eigenmodes and resistive interchange modes excited in NB-heated high beta plasmas of LHD

Figure 3 shows a typical discharge with TAEs obtained at B_t=0.6T (CCW direction) in the magnetic configuration of R_{ax} =3.6 m. In this shot, three tangential NBs are tangentially injected. The electron temperature at the centre T_{e0} is ~0.8 keV, and line-averaged electron density $<n_e>$ is ~1.5×10^{19}m^{-3}. The volume-averaged beta value $<\beta>$ is relatively high ~2.0 %, as seen from Fig.3a. The ratio of gyroradius of beam ions to averaged plasma minor radius $\rho_h/<a>$ is fairly large. i.e., ~0.15 m/0.6 m.   The ratio of the initial energetic-ion velocity to the Alfvén speed is v_h/v_A~2. The volume-averaged energetic-ion beta value $<\beta_h>$ is comparable to $<\beta>$, estimated to be ~1 %, on the assumption of classical slowing down of beam ions for ~5 MW beam deposition. Strongly excited TAE and RICs are identified in the quasi-stationary phase (2.8s $\leq t \leq$ 3.2s) from the spectrogram analysis of magnetic probe signal. In high β plasmas in the inward-shifted configuration (R_{ax}=3.6 m), TAE and low-frequency RICs often coexist. RICs are excited near the plasma edge due to the steep gradient of bulk plasma pressure and can generate a magnetic island in nonlinear evolution regime, while linearly unstable interchange has no magnetic island [35]. The radial structure of the RICs can be derived from the data of SX/AXUV detector arrays [36-38].

In this paper, the discharge at t~2.82 s is mainly discussed. The radial profiles of electron temperature T_e and n_e measured with Thomson scattering diagnostic (TSD) at this time are shown in Fig.4a. Hydrogen atom density n_0 is assumed to be scaled as $1/n_e^2$, of which

scaling was derived from the experimental result on the CHS having a similar magnetic configuration [39]. As seen from Fig.4a, n_o does not change significantly toward the last closed flux surface ($r/a=1$) and would rapidly decrease from the value at the edge of ergodic layer where electron density and temperature are very low. The deposition profile of NB-generated energetic ions is shown in Fig. 4b. It is calculated using FIT code [40], which gives the deposition profile of beam ions averaged over the magnetic surface taking into account the prompt orbit loss. The MHD equilibrium is reconstructed using experimental data by VMEC2000 code [41] in the free boundary condition. The reconstruction of MHD equilibrium was done using the pressure profile evaluated from the experimentally obtained data on the assumption of $T_e=T_i$ and $n_e=n_i$ having a multiplication factor of energetic ion effect (in this case, the factor is ~1.2) so that the calculated magnetic axis position agrees well with that predicted from T_e-profile.

The scintillator image in the time frame of t=2.820-2.822 s captured by a CMOS camera is shown in Fig.5a. On this image, three-primary-loss domains, named D_1, D_2 and D_3, are clearly recognized. Lost energetic ions of [$\rho_h(E)$, χ]=[11-15 cm(80-150keV), 25-35 deg.], [8-18 cm (50-190keV), 35-45 deg.] and [8-18 cm (50-190 keV), 45-60 deg.] would reach the domain D_1, D_2 and D_3, respectively. Here, $\rho_h(E)$ is evaluated using B_{SLIP}= 0.37 T. The scintillation image expands into the region of ρ_h>17 cm (E>190 keV), especially in D_3 domain,

although E_b is less than 190 keV. This is due to relatively low energy-resolution of the SLIP, typically ~±20 keV for E/χ = 150 keV/60 degrees, even larger for higher energy ions. The orbit calculation indicated that energetic ions have passing, passing, and passing - toroidally trapped (or so-called "transition") orbits would reach D_1, D_2, and D_3 domains, respectively. On the other hand, Fig.5b shows these loss fluxes monitored with 16 PMTs of which frequency responses are 20 kHz for No's. 1~6, 8, 11, 12, 14, 15 and 16 PMTs and 200 kHz for No's. 7, 9, 10 and 13 PMTs. As seen from Figs. 5a and 5b, TAE/RIC-induced losses are dominantly detected on the above-mentioned three domains D_1, D_2 and D_3. The RIC-induced loss and TAE-induced one are mainly detected on D_1 and D_2, respectively. Loss flux detected on D_3 is mainly caused by Coulomb collisions in the non-uniform magnetic field structure, since the D_3 region is observed even in the phases without TAE and RICs. In subsequent sub-sections, effects of respective MHD instability, TAE or RIC on beam-ion losses will be discussed in detail.

3.2 Beam-Ion Losses due to TAE

Strongly excited TAE having 60~80 kHz is observed in the time window from t~2.7 s to 3.3 s by means of MPs, as shown in Fig.3. The toroidal and poloidal mode numbers are n=1 and m~1, respectively. The values of n and m were determined by MPs. The amplitude of TAE evaluated at the MP position is ~5×10^{-5} T at t=2.82 s. Shear Alfvén continua calculated by

STELLGAP code [42] is shown in Figure 6a. A TAE eigenfunction is calculated using AE3D

code [43] for m=0~10 assuming that ion density $n_i = n_e$ and MHD equilibrium is reconstructed

using VMEC2000 (Fig.4). As seen from Fig.6b, eigenfunction of the observed TAE is

composed by two dominant Fourier components and have a similar character of a core-localized

TAE which can exist in low magnetic shear region of a tokamak plasma. This TAE is the odd

parity mode, and has the peak of the eigenfunction at normalized radial position r/a ~0.6.

Unlike tokamaks [44], the TAE with odd parity is often strongly excited having large

amplitude in LHD. Although the reason is not clarified yet at this moment, it may be attributed

to strong continuum damping at the very edge of the plasma having high magnetic shear for an

even parity TAE, as seen from the character of the TAE gap near the edge shown in Fig.6a. In

high-n and analytic approximation, the continuum damping rate increases strongly with the

increase in the magnetic shear strength [45]. Moreover, the continuum damping rate for low-n

TAE increases more rapidly with the increase in the magnetic shear strength, compared with

that for high-n TAE [46- 48]. This may be a dominant cause that even TAE is usually

suppressed or only be very weakly destabilized.   A detailed numerical calculation is required to

draw a decisive conclusion on the difference in excitation of even and odd parity TAEs, and is

left for a future work.

Fluctuations of n_e due to TAE are observed as Hα fluctuations by FHA diagnostics in

LHD plasmas at fairly low B_t (typically <1 T). The information of the radial structure of TAE can be derived through the cross correlation between the Hα fluctuation $\tilde{I}_{H\alpha}$ signal and the MP signal $d\tilde{b}_\theta/dt$ [33]. The fluctuation components modulated by TAE in $\tilde{I}_{H\alpha}$ was calculated by the product of the coherence $\gamma^2_{H\alpha-MP}$ and the power spectral density of $\tilde{I}_{H\alpha}$, where the coherence between TAE induced fluctuations and background fluctuations due to edge turbulence is assumed to be negligibly small [49]. Thus derived TAE induced Hα fluctuations integrated along the line of sight is shown in Fig.7c. On the other hand, the predicted Hα fluctuations were calculated by TAE eigenfunctions obtained by AE3D code (Fig.6) and plasma parameters including assumed neutral density profile shown in Fig.4. The predicted electron density fluctuations were obtained based on ideal MHD theory. The plasma displacement due to shear Alfvén waves such as TAE was evaluated under the condition that the magnetic perturbations are expected to be purely transverse. Each local Hα emission patterns (Hα emissibility) induced by m=1 and m=2 Fourier components in TAE eigenfunction in circular plasma are shown in Fig.7a. The local Hα emission induced by whole TAE eigenfunction is given in Fig.7b, on the assumption that the mode pattern of local Hα emission is uniform in the toroidal direction. The Z-profile of Hα emission integrated along the sight lines shown in Fig.1c in the Z-direction is shown as the profile of the normalized minor radius (Fig.7c). The detailed equations used for this calculation are given in Appendix 1. Thus calculated profile agrees well

with the structure obtained using FHA. This result indicates that this FHA diagnostics newly

introduced on LHD has a potentiality to give useful information on the internal structure of

TAEs excited in high beta plasmas characterized by relatively high density at considerably low

toroidal field.

As shown in Fig.8a, the sharp drop and relatively slow rise in the charge-exchanged

fast-neutral fluxes Γ_{neutral} in the range of energy from 180 keV to 190 keV are observed,

correlating with each TAE burst, while Γ_{neutral} in the range of E=130 keV to 160 keV exhibits a

rapid rise and slow decay. The temporal evolution of charge-exchanged neutral fluxes will

indicate the effect of the clump-hole pair creation in velocity space caused by TAE burst [50].

The time evolution of $\Gamma_{\text{neutral}}(E$=130-160keV) related to the clump formation indicates the rapid

radial transport of energetic ions, suffering from rapid changes in ion energy and pitch angle,

and would be lost outside the plasma during the process. The loss flux of energetic ions detected

on the D_2 domain of SLIP has a similar shape of the pulse. The characteristic decay time of the

beam-ion loss flux to SLIP Γ_{SLIP_10} is evaluated to be ~4.5 ms that is comparable to the

estimated slowing down time through Coulomb collision of beam ions with electrons (~5 ms) at

the peak of the TAE eigenfunction without TAE. During the slowing down of the formed clump

of energetic ions between TAE bursts, some amount of the ions will be lost and detected by

SLIP. This process would lead to the slow decay of the SLIP signal Γ_{SLIP_10} shown in Fig.8a.

These observations tell us that substantial transport/loss of energetic ions is induced by TAEs.

That is, the peak just after the TAE burst is thought to be caused by the TAE burst. It should be

noted that the signal $\Gamma_{\text{SLIP\_10}}$ is also modulated more frequently, compared with the change by

TAE burst. This frequent modulation is caused by the RIC mode excited near the plasma edge

[25], and will be discussed in more detail in the next sub-section. After the frequent modulations

due to RIC modes in $\Gamma_{\text{SLIP\_10}}$ was removed using numerical band-pass filter, the increment of the

beam-ion loss rate due to TAE bursts $\Delta\Gamma_{SLIP}$ was evaluated. Moreover, time averaging every 10

μs time interval was also applied to remove remaining white noise in $\Gamma_{\text{SLIP\_10}}$. Thus derived

smoothed $\Gamma_{\text{SLIP\_10}}$ is also overlaid in the trace of $\Gamma_{\text{SLIP\_10}}$. In Fig. 8b, $\Delta\Gamma_{SLIP}$ evaluated with the

difference of $\Gamma_{\text{SLIP\_10}}$ between the pulse peak and that just before each TAE burst is plotted

versus the magnetic fluctuation amplitude measured at the MP position. The error bar

corresponds to the level of the white noise. In this figure, the curve of $\Delta\Gamma_{SLIP} \propto (\tilde{\tilde{b}}_{TAE})^2$ is also

shown. As seen from Fig.8b, $\Delta\Gamma_{SLIP}$ induced by TAE increases non-linearly or approximately

quadratically with the increase in the TAE magnetic fluctuation amplitude, although the data

points are scattered appreciably. This may suggest a diffusive-type loss rather than a convective

one [51]. These energetic ions may not be lost promptly from the plasma region by TAE.

Presumably, first, energetic ions would be transported by TAE excited around $r/a \sim 0.6$ to the

plasma edge region, as discussed in refs. [50, 52], being scattered into the loss orbit.

The temporal changes of E and χ associated with TAE burst may be obtained through comparison among the loss flux signals ($\Gamma_{\text{SLIP\_1}}$, $\Gamma_{\text{SLIP\_2}}$, ... $\Gamma_{\text{SLIP\_16}}$) having various E and χ. Temporal evolutions of $\Gamma_{\text{SLIP\_14}}$, $\Gamma_{\text{SLIP\_13}}$, $\Gamma_{\text{SLIP\_10}}$ and $\Gamma_{\text{SLIP\_6}}$ are shown together with NPA signals in Fig. 9a. The signals $\Gamma_{\text{SLIP\_10}}$ and $\Gamma_{\text{SLIP\_6}}$ and charge-exchanged fast neutral having E=130 keV $\Gamma_{\text{neutral\_E=130keV}}$ are rapidly increase and slowly decay by TAE burst exhibiting similar wave forms, although $\Gamma_{\text{SLIP\_6}}$ is appreciably deformed by RICs. In contrast to them, the signals $\Gamma_{\text{SLIP\_13}}$ and $\Gamma_{\text{SLIP\_14}}$ and charge-exchanged fast neutral having E>180 keV $\Gamma_{\text{neutral\_E>180keV}}$ suddenly decrease and slowly recover by TAE burst, having similar wave forms. That is, the hole formation in the velocity space by TAE burst is seen as a sharp drop on the wave of $\Gamma_{\text{neutral\_E>180keV}}$ which will be proportional to source signal of energetic ions supplied by NBI. Energetic ions in this energy range will also be lost by TAE burst suffering from a certain change of the pitch angle, which will be detected as $\Gamma_{\text{SLIP\_14}}$ and $\Gamma_{\text{SLIP\_13}}$. At the same time with the hole formation, the formed clump with a certain energy drop is recognized as a pulsed increase in the signal $\Gamma_{\text{neutral\_E=130keV}}$. Thus generated energetic ions with some energy drop will be lost and be detected as $\Gamma_{\text{SLIP\_6}}$ and $\Gamma_{\text{SLIP\_10}}$. The above mentioned characters in these signals indicate clearly that the E and χ of lost ions are quickly changed during each TAE burst. This is also clearly seen on the scintillation pattern shown in Fig.9b. If fast ions are kicked by TAE into another position, this may lead to another loss orbit. The increase in $\Gamma_{\text{SLIP\_6}}$ by TAE burst

15

shows a certain time lag for that in $\Gamma_{\text{SLIP\_10}}$, although the signal seems to be still deformed by

RIC induced losses. This time lag suggests that further pitch-angle scattering by TAE bursts

needs a certain time.

Interestingly, high-frequency fluctuations of Γ_{SLIP} correlated with TAE mode

frequency (~70 kHz) were observed using correlation analysis between Γ_{SLIP} and the MP signal,

as seen from the spectrogram of the coherence shown in Fig.10a. High-frequency ion loss fluxes

correlated with TAE are often observed in the ranges of the energy and the pitch angle of lost

ions: E/χ~180 keV/45-55 degrees and 6 - 23 keV/25-35 degrees. The E and χ ranges match to

the regions indicated by red circles in Fig.10b. The energy of lost energetic ions in the regions

#5 and #15 shown in Fig. 10b respectively satisfies the fundamental and the sideband resonance

conditions of TAE, that is $v_{//} \geq v_A$ and $\geq v_A/3$ at TAE mode peak [53]. The Alfvén speed at the

peak position of the TAE eigenfunction ($r/a \sim 0.6$) is ~2.2×10^6 m/s. The $v_{//}$ of lost beam ions at

the region #5 ~3.4×10^6 m/s (ρ_h~15 cm, χ~50 degrees and B_{SLIP} at SLIP position is 0.37 T)

corresponds to $v_{//}/v_A$~1.5. The velocity at # 15 ~ 9.2×10^5 m/s ($\rho_h \sim 5$ cm, $\chi \sim 30$ degrees)

corresponds to $v_{//}/v_A$ ~0.4. The fluctuations in Γ_{SLIP} suggest the existence of fundamental and

side-band resonant interactions between TAE and energetic ions.

3.3 Energetic-Ion Losses due to RIC

16

As mentioned briefly in the previous sub-section, these low frequency instabilities also induce energetic ion losses, which are clearly detected by SLIP. In this high beta shot RIC with m/n=1/1 is strongly excited. The mode frequency of about 2 kHz is related to mainly poloidal plasma rotation (Fig.3b). Fluctuations in AXUV signals in the frequency range of 1.5~2.5 kHz would give the information of the eigenfunction of m/n=1/1 RIC mode. The radial profiles of the AXUV fluctuation amplitude related to m/n=1/1 RIC mode in the time window of t=2.75~2.83 s are shown in Fig.11a, together with the fitted AXUV fluctuation data obtained using a model profile of the local emissivity of AXUV. In this analysis, the parameters x_o and w in the model function $\exp[\{(r/a-x_0)/w\}^2]$ were adjusted so that the calculated AXUV fluctuation profile taking account the line of sights of the AXUV detector array (Fig.1d) should best-fit to the experimental data [37]. Here, x_o and w correspond to the location of the rational surface and the island width. The model function of the local emissivity corresponds to the radial structure of the m/n=1/1 RIC mode. The best fit result was obtained with x_0=0.9 and w=0.2. Figure 11b shows the thus obtained radial profile of the emissivity fluctuation caused by m/n=1/1 RIC mode. The peak position x_0 agrees well with the position of $\iota/2\pi = 1$ rational surface shown in Fig. 4b. This approximately corresponds to the eigenfunction of the RIC mode. On the other hand, the dispersion relation of RIC is given in Appendix 2 and eigenmode function can be derived from the eigenmode equation. In the present paper, however, we did not make direct

17

comparison of the RIC-induced fluctuation profile derived from experimental data (Fig.11b)

with the eigenfunction calculated from the RIC eigenmode equation, because the experimentally

obtained eigenfunction is applicable to qualitative discussion on interaction of the RIC mode

with energetic ions.

Energetic-ion losses induced by RIC are mainly observed in the domains D_1 and D_3 on

the ρ_h -χ plane shown in Fig.5a. Energetic-ion loss fluxes are increased and modulated

synchronizing with the RIC mode oscillation as seen from Figs. 5 b. The zoomed time

evolutions of the magnetic fluctuation of RIC and the beam-ion loss flux signals Γ_{SLIP_6} and

Γ_{SLIP_13} are shown in Fig.12a. The pitch angle χ of these lost-beam ions is close to that of the

so-called transition particles of which orbit randomly changes between co-passing and

toroidally trapped orbits[54] . It should be noted that the particle gyro radius ρ_h correspond to

the ions with slightly reduced energy from the injection energy of NB. Fluctuations of Γ_{SLIP}

correlated with RIC were observed using coherence analysis (Fig 12 b). It should be noted that

Γ_{SLIP} fluctuation is not only correlated with fundamental RIC mode of ~2kHz but also the

second harmonic having ~ 4 kHz (Fig 12 b and Fig 3 b). Moreover, it is clearly found from the

phase analysis that the phase difference between Γ_{SLIP_13} and RIC is approximately fixed at

~185° having appreciable variation of about ±50° (Fig 12 c). The reason why the phase does

not stay rigorously constant is thought that RIC induced losses would be induced through

stochastization of energetic ion orbit due to large amplitude RIC oscillations. The increment of

loss fluxes due to RICs increases linearly rather than non-linearly with the magnetic fluctuation

amplitude, as shown in Fig. 12d. This dependence suggests a convective-type loss [51].

In edge region of LHD, plasma rotates mainly in the poloidal direction due to high

toroidal viscosity. The $m/n=1/1$ RIC mode frequency of ~2 kHz will reflect the poloidal plasma

rotation. In this situation, we discuss whether or not trapped energetic ions could interact with

this mode. The resonance condition for helically trapped ion is $\omega \sim N\Omega$ where ω and Ω indicate

the frequency of the mode and the toroidal precession frequency, and N is the harmonics number

[4]. Note that in LHD configuration, once energetic ions are deeply trapped in a helical ripple

well, those ions can drift toroidally while they rotate poloidally along the valley of the two

helical winding coils [55, 56]. The poloidal precession of helically trapped ion ω_{hp} is expressed

as [57], $\omega_{hp} = -2l\left(\dfrac{E(\kappa)}{K(\kappa)} - \dfrac{1}{2}\right)\varepsilon_h\omega_0$, where $\kappa^2 \approx \dfrac{1}{2\varepsilon_h}\dfrac{v_{//}^2}{v_\perp^2}$, $\omega_0 = \dfrac{-E}{B_0 r^2}(\iota/2\pi)$, and

$E = \dfrac{1}{2}m_h v_\perp^2$. Here, $E(\kappa)$ and $K(\kappa)$ represent the first and the second kinds of the complete

elliptic integrals, respectively. The parameter ε_h stands for the ratio of amplitude of

fundamental helical perturbation component B_{21} to magnetic field strength $B_{00,}$ where two

subscripts of the field amplitude stand for the poloidal and toroidal numbers of the helical field.

The B_0 is the strength of the resultant magnetic field strength, i.e., $B_0 \approx B_{00}$. For simplicity, we

discuss the deeply helically trapped limit, that is, $v_{//} \sim 0$. The minor radius and magnetic field

strength are chosen as the peak position of RIC: $r = 0.54$ m and $B_0 = 0.6$ T, respectively. Since

the toroidal precession frequency of helically trapped particle ω_{ht} is approximately expressed as

$\omega_{ht}=(l/M) \bullet \omega_{hp}$, ω_{ht} is estimated to be ~10 kHz for helically trapped ion of E=130 keV using $\varepsilon_h =$

0.2, which is the value at $r/a = 0.9$ in the present plasma condition [53]. Since ω_{hp} is much

higher than the mode frequency (~2 kHz), trapped ion would not to be a candidate for the

resonant interaction. However, this kind of resonant interaction may not be ruled out

completely, because the above discussion is still crude and more detailed particle orbit

calculations are needed. Again, it should be noted that toroidally trapped energetic ions is an

extremely small fraction of energetic ions in LHD because of tangential beam injection and the

relatively large aspect ratio of the plasma (R_0/r~6).

As another more likely mechanism, energetic ions travelling near the plasma edge as

shown in Fig.1a may suffer from falling into an escaping orbit easily by the large amplitude of

magnetic fluctuations of RIC mode near the edge, of which magnetic fluctuations are related to

the eigenfunction shown in Fig.11b (r/a~0.9) [37]. This loss is thought to be caused by

stochastization of the orbit of energetic ion by RICs.

4. Summary

In NB-heated plasmas in LHD, anomalous losses of energetic-ions due to TAE and

RIC modes were observed using the SLIP placed at the outboard side of LHD. The radial profile of Hα-fluctuations due to TAE was derived through correlation analysis between Hα fluctuations and magnetic fluctuations. The radial structure of Hα fluctuations calculated using the eigenfunction of TAE obtained with AE3D code agrees well with the experimentally obtained Hα fluctuation profile. This comparison has demonstrated that the FHA newly installed on LHD is a powerful diagnostic tool to get information of the TAE internal structure in high beta plasmas obtained at considerably low toroidal field. Energetic ions lost by TAE bursts belong to a class of co-passing particles. From the temporal analysis of SLIP signals obtained by multi PMTs, it was shown that E and χ of the lost-energetic ions are quickly changed by each TAE burst. The relation between the magnetic fluctuation amplitude and the increment of loss flux by TAE is approximately quadratic and suggests diffusive type loss. High-frequency fluctuation components in energetic ion loss flux correlated with TAE oscillations were clearly observed at the energy range in co-passing orbits where the resonance conditions of the fundamental and the sideband excitation of TAE are satisfied. In addition to TAE, enhanced losses of energetic ions due to RIC were recognized in the vicinity of passing and toroidally trapped boundary for energetic ions, where the RIC has the peak near the plasma edge. The dependence of the RIC induced losses on the magnetic fluctuation amplitude is nearly linear and suggests convective type loss. Numerical simulations are required to clarify the details of loss

processes of energetic ions induced by TAEs or RICs. Moreover, synergistic effects of TAEs and

RICs on energetic ion losses are also important for LHD plasmas, and would be also important

for tokamak plasmas. This is one of future interesting research targets.

Acknowledgements

Appendix 1

The amplitude of Hα fluctuations $\tilde{I}_{H\alpha\text{-}AE}$ induced by AE is expressed as,

$$\tilde{I}_{\text{H}\alpha\text{-AE}} \cong \int \overline{\left(n_0 n_{\text{e}} \left\langle \sigma_{\text{ex}} v_{\text{e}} \right\rangle\right)}_{\text{AE}} dl \tag{A1}$$

where, n_0, n_{e}, l, and $\langle\sigma_{ex}v_e\rangle$ indicate neutral density, electron density, the path length along the

sight line of an Hα detector, and electron-impact excitation rate coefficient averaged over the

Maxwell distribution function. The subscript AE stands for the contribution from AE activities.

In this formula, fluctuations of neutral density and $\langle\sigma_{ex}v_e\rangle$ is assumed to neglected because of

T_e is the range from 10 eV to 700 eV in the present experimental condition, then

$$\tilde{I}_{\text{H}\alpha\text{-AE}} \cong \int n_0 \tilde{n}_{\text{e-AE}} \left\langle \sigma_{ex} v_e \right\rangle dl \propto \int n_0 \tilde{n}_{\text{e-AE}} dl \tag{A2}$$

In Eq. (A2) $\langle\sigma_{ex}v_e\rangle$ is almost constant in this T_e range. Accordingly, Hα fluctuations will reflect electron density fluctuation and profiles of neutral density.

According to Ideal MHD theory, fluctuation of electron density due to plasma displacement ξ is expressed as

$$\tilde{n}_e \cong -n_e \nabla \cdot \xi - \xi \cdot \nabla n_e . \tag{A3}$$

From Eqs. (A2) and (A3), the Hα fluctuation induced by the displacement related to AE ξ_{AE} is expressed as,

$$\tilde{I}_{H\alpha-AE} = \int n_0 \left(-n_e \nabla \cdot \xi_{\text{AE}} - \xi_{\text{AE}} \cdot \nabla n_e \right) dl \tag{A4}$$

On the other hand, shear Alfvén wave may be approximated by a transverse magnetic perturbations and the condition is expressed as,

$$\mathbf{B}_0 \cdot \delta \mathbf{B} = -\mathbf{B}_0^2 \left(\nabla \cdot \xi \right) - \mathbf{B}_0 \cdot \left(\xi \cdot \nabla \right) \mathbf{B}_0 + \mathbf{B}_0 \cdot \left(\mathbf{B}_0 \cdot \nabla \right) \xi = 0 \tag{A5}$$

where, B_0 and δB indicate equilibrium magnetic field and the magnetic perturbation induced by shear Alfvén wave, respectively. On the assumption of strong toroidal field, $\nabla \cdot \xi_{AE} \cong \dfrac{2}{R} \xi_{R\_AE}$ is derived from Eq.(A5), where R is the major radius. This relation agrees with that shown in the ref [58] through more rigorous treatment. Taking into account that the electron density

gradient is r (radial) direction, the equation (A4) is modified as,

$$\tilde{I}_{H\alpha-AE} = \int n_0 \left(-\frac{2}{R} n_e \xi_R - \frac{dn_e}{dr} \xi_r \right) dl \qquad (A6)$$

The displacement induced by TAE is approximately derived from the scalar potential obtained from AE3D code as,

$$\boldsymbol{\xi}_{AE} = \int \mathbf{v}_k dt \approx -\int \frac{(\mathbf{e}_k \times \mathbf{B})}{B^2} dt = -\int \frac{(\nabla \phi_k \times \mathbf{B})}{B^2} dt = -\frac{i}{\omega} \frac{\phi_k (\mathbf{k} \times \mathbf{B})}{B^2} \qquad (A7)$$

where k, $\mathbf{v}$, $\mathbf{e}$, ϕ, $\mathbf{B}$ and ω indicate wave number, velocity, electrical field induced by TAE, the electrostatic potential, magnetic field strength and the TAE frequency. With large aspect ratio approximation ($R \gg r$), the displacement for TAE in cylindrical coordinate (r, φ, θ) with low n can be simply expressed as,

$$\xi_R \sim \frac{1}{\omega} \left(\frac{m\cos\theta}{B_{\varphi0}} \frac{\phi}{r} - i \frac{\sin\theta}{B_\varphi} \frac{\partial\phi}{\partial r} \right) \qquad (A8)$$

$$\xi_r \sim i \frac{m\phi}{r\omega B_\varphi} \qquad (A9)$$

where $i = \sqrt{-1}$ then, (A6) is rewritten as

$$\tilde{I}_{H\alpha-AE} \sim \frac{1}{\omega} \int \frac{n_0}{B_\varphi} \left\{ -\frac{2}{R} n_e \left(m\cos\theta \frac{\phi}{r} - i\sin\theta \frac{\partial\phi}{\partial r} \right) + \frac{dn_e}{dr} \frac{m\phi}{r} \right\} dl \qquad (A10)$$

Hence, the amplitude of Hα fluctuation is expressed as

$$\tilde{I}_{H\alpha-AE\_rms} \sim \frac{1}{\omega} \int \frac{n_0}{B_\varphi} \left\{ \sqrt{\frac{m^2\phi^2}{r^2} \left(\frac{dn_e}{dr} - \frac{2}{R} n_e \cos\theta \right)^2 + \left(\frac{2}{R} n_e \sin\theta \frac{\partial\phi}{\partial r} \right)^2} \right\} dl. \qquad (A11)$$

Appendix 2

The dispersion relation of RIC mode in cylindrical plasma is given as follows [59]

$$2\rho\left(1+\frac{g-\omega_*}{\omega}+\rho^2\frac{m^2}{r^2}\right)=\pi e^{i3\pi/4}\frac{(\nu\omega)^{1/2}}{\varepsilon\left|k_{//}^{'}\right|}\left(\frac{g\omega_*}{\omega^2}+\rho\frac{m^2}{r^2}\right) \tag{A12}$$

$$\rho=\rho_s/a \tag{A13}$$

$$g=\frac{m}{r}\frac{d\Omega}{dr} \tag{A14}$$

$$\omega_*=-\frac{m}{r}\frac{1}{n_0}\frac{dn_0}{dr} \tag{A15}$$

$$k_{//}^{'}=(m\iota-n)/(r-r_0) \tag{A16}$$

where, ν, ε, ω, ρ_s, a, Ω, r, r_0, m, and n indicate ion-electron collision frequency normalized by

electron cyclotron frequency, inverse of aspect ratio, frequency of the mode, bulk ion Larmour

radius evaluated with the electron temperature, plasma minor radius, the curvature of magnetic

field, radial position, the location of the rotational surface, poloidal mode number and toroidal

mode number, respectively. Index of "0" indicates the rational surface. The mode is interchange

type and therefore localizes around the rotational transform ($\iota/2\pi = 1/q$: q is safety factor).

References

25

[1]   Fasoli A., Gormenzano C., Berk H. K. *et al*., Progress in the ITER Physics Basis Chapter 5:

       Physics of energetic ions 2007 Nucl. Fusion **47**, S264

[2]   Chen C. Z. and Chance M. S., 1986 Phys. Fluids **29**, 3695

[3]   Chen L., 1994 Phys. Plasmas **1**, 1519

[4]   Mynick H. E., 1993 Phys. Fluids B **5** 5

[5]   Sigmar D.J., Hus C.T., White R. *et al*, 1992 Phys. Fluids B **4** 6

[6]   Heidbrink W.W. and Sadler G.J, 1994 Nucl. Fusion **34** 4 535

[7]   Darrow D. S., Zweben S. J, Chang Z. *et al*, 1997 Nucl. Fusion **37** 7 939

[8]   Kimura H., Kusama Y., Saigusa M., *et al*., 1998 Nucl. Fusion **38** 9 1303

[9]   Shinohara K., Kusama Y., Takechi M. *et al*, 2001 Nucl. Fusion **41** 5 603

[10] Zweben S.J., 1989 Nucl. Fusion **29** 5 825

[11] Darrow D.S., Herrmann H. W., Johnson D. W *et al*., 1995 Rev Sci. Instrum. **66** 476

[12] Todo Y., Berk H. L. and Breizman B. N., 2003 Phys. Plasmas **10** 7

[13] Briguglio S., Fogaccia G., Vlad G. *et al*, 2007 Phys. Plasmas **14** 055904

[14] Stratton B. C., Fonck R.J., Mckee G. R. *et al*., 1996 Nucl. Fusion **36** 11 1586

[15] Lovberg J. A., Heidbrink W. W., Strachan J. D. *et al*., 1989 Phys. Fluids B **1** 4

[16] Marcus F. B., Adams J. M., Bond D. S. *et al*., 1994 Nucl. Fusion **34** 5 687

[17] Carolipio E.M., Heidbrink W. W., Forest C.B. *et al*, 2002 Nucl Fusion **42** 853

[18] García-Muñoz M., Martin P., Fahrbach H.U. *et al*., 2007 Nucl. Fusion **47** L10

[19] Darrow D. S., 2008 Rev. Sci. Instrum. **79** 023502

[20] García-Muñoz M. , Fahrbach H.U.,and Zohm H., 2009 Rev. Sci. Instrum. **80** 053503

[21] Baeumel S., Werner A., Semler R., *et al*., 2004 Rev. Sci. Instrum. **75** 3563

[22] Isobe M., Darrow D. S., Kondo T. *et al*., 1999 Rev. Sci. Instrum. **70** 827

[23] Isobe M., Toi, K., Matsushita, H. *et al*., 2006 Nucl. Fusion **46** S918.

[24] Werner A., Weller A., Darrow D. S. *et al*, 2001 Rev. Sci. Instrum. **72** 1 780

[25] Watanabe F., Satoshi O., Shohji T. *et al*., 2005 J. Plasma Fusion Res. **81** 967

[26] Ogawa K., Isobe M. and Toi K., 2009 J. Plasma Fusion Res. Series **8** 655

[27] Ogawa K., Isobe M. and Toi K., 2008 Plasma Fusion Res. **3** S1082

[28] Ogawa K., Isobe M., Toi K., *et al*. 2009 Plasma and Fusion Res. **4** 033

[29] Toi K., Yamamoto S., Nakajima N. *et al*., 2004 Plasma Phys. Control. Fusion **46** S1.

[30] Toi K., Isobe M., Osakabe M. *et al*., to be published in 2010 Fusion Science and Technology.

[31] Isobe M. Osakabe M., Ozaki T. *et al*., to be published in 2010 Fusion Science and Technology.

[32] Takahashi H., Sakakibara S., Kubota Y. *et al*., 2001 Rev. Sci. Instrum. **72** 3249

[33] Ogawa K., Toi K., Isobe M. *et al*., 2008 Plasma Fusion Res. **3** 030

[34] Watanabe F., Toi K., Ohsachi S. *et al*., 2007 Plasma Fusion Res **2** S1066

[35] Ichiguchi K., Nakajima N., Wakatani M. *et al*., 2003 **43** 1101

[36] Watanabe F., Toi K., Ohdachi S. *et al*., 2008 Nucl. Fusion **48** 024010

[37] Watanabe F., Toi K., Ohdachi S. *et al*., to be published in Contributions to Plasma Phys. 2009

[38] Watanabe F., Toi K., Ohdachi S. *et al*., 2006 Plasma Phys. Control. Fusion **48**, A201

[39] Takenaga H., Nakao T, Uchino K. *et al,*. 1995 Nucl. Fusion **35** 1 107

[40] Murakami S., Nakajima N., Okamoto M. *et al*., 1995 Trans. Fusion Technol. **27** 256

[41] Hirshman S. P. and O. Betancourt, 1991 J. Comput. Phys. **96** 99

[42] Spong D.A. Hirshman S., Lyon J. *et al*., 1999 Bull. Am. Phys. Soc. **44** 215

[43] Spong D.A., D'Azevedo E. and Todo Y., 2010 Phys. Plasmas **17** 022106

[44] Kramer G. J., Sharapov S.E., Nazikian R. *et al*., 2004 Phys. Rev. Lett. **92** 015001

[45] Rosenbluth M. N., Berk H. L., Van Dam J. W. *et al* 1992 Phys. Rev. Lett. **68** 5 596

[46] Fu G.Y., Cheng C. Z. Budny R. *et al*., 1993 Phys. Fluids B**5** 4040

[47] Berk H. L., Van Dam J. W., Guo Z and Lindberg D. M., 1992 Phys. Fluids B **4** 7 1806

[48] Strait E. J., Heidbrink W. W., Turnbull A. D. *et al*., 1993 Nucl. Fusion **33** 12 1849

[49] Ikeda R., Toi K., Takeuchi M., *et al* 2008 Phys. Plasmas **15** 072505

[50] Osakabe M., Yamamoto S., Toi K. *et al*., 2006 Nucl. Fusion **46** S911-S917

[51] Heidbrink W.W., Doung H. H., Manson J. *et al*., 1993 Phys. Fluids B **5** 2176

[52] Todo Y., Nakajima N., Osakabe M. *et al*., 2008 Plasma Fusion Res. **3**, S1074-1 1661

[53] Berk H. L., Breizman B. N., Perkker M. S. *et al*., 1995 Nucl. Fusion **35** 15

[54] Wakatani M., 1998, "Stellarator and Heliotron Devices", Oxford University Press, New

York, Chap.6

[55] Murakami S., Wakasa A., Maaβberg H. *et al*., 2002 Nucl. Fusion **42** L19-L22

[56] Mynick H. E., Chu. T. K. and Boozer A. H., 1981 Phys. Rev. Lett. **48** 322

[57] Miyamoto K., 1989 "Plasma physics for nuclear fusion", Revised edition, The MIT press,

Cambridge, Mass.

[58] Nazikian R., Kramer G. J., Cheng C. Z. *et al*., 2003 Phys. Rev. Lett. **91**, 125003

[59] Sugama H. Wakatani M. Hasegawa A., 1988 Phys. Fluids **31** 6
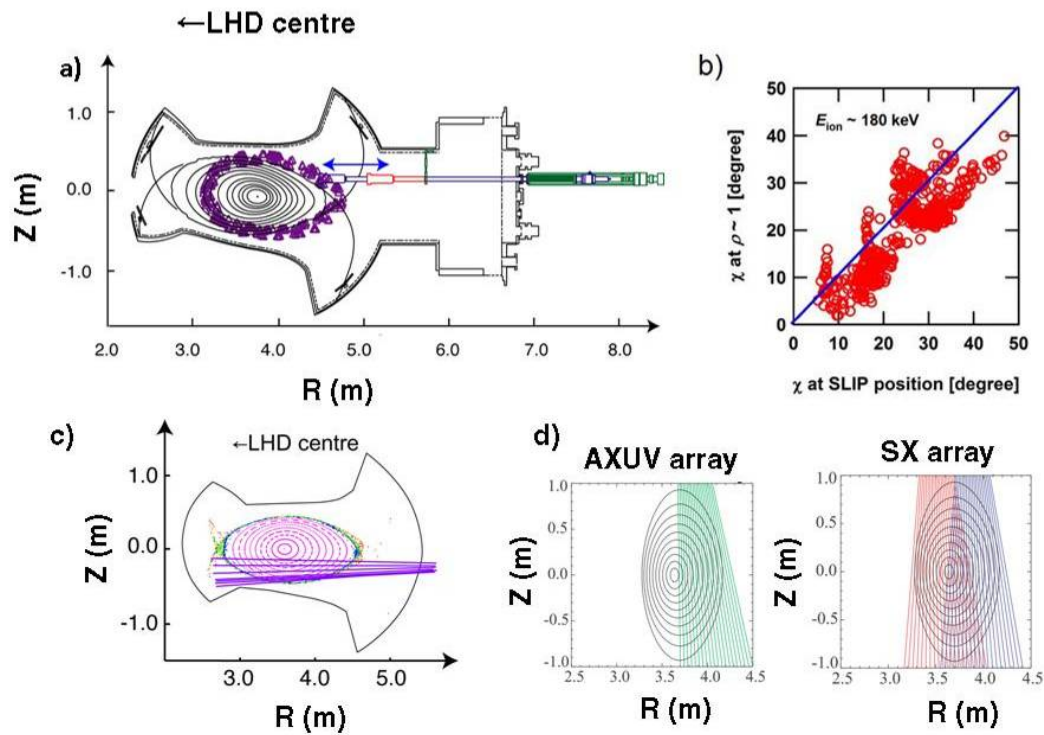
Fig. 1 a) Schematic drawing of the SLIP installed on the outboard side of the LHD and a

Poincaré plot of the typical orbit which can be detected with the SLIP. The orbit of the

detectable ion deviates from magnetic flux surfaces. b) The relationship between the pitch angle

of energetic ions at the SLIP position and that on the plasma surface. The pitch angle on the

plasma surface was evaluated by calculating the orbit of energetic ions launched from the SLIP

in the vacuum field. c) The sight lines of FHA, where FHA consists of seven PMTs having fast

time response up to 5 μs. d) Sight lines of AXUV array and SX array, each array consists of

twenty detectors.
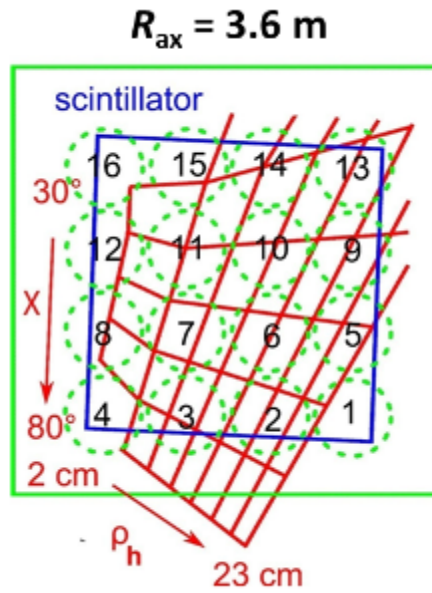
Fig. 2 E/χ map on the scintillator screen. The circles 1 to 16 on the screen indicate the area that

each PMT views.
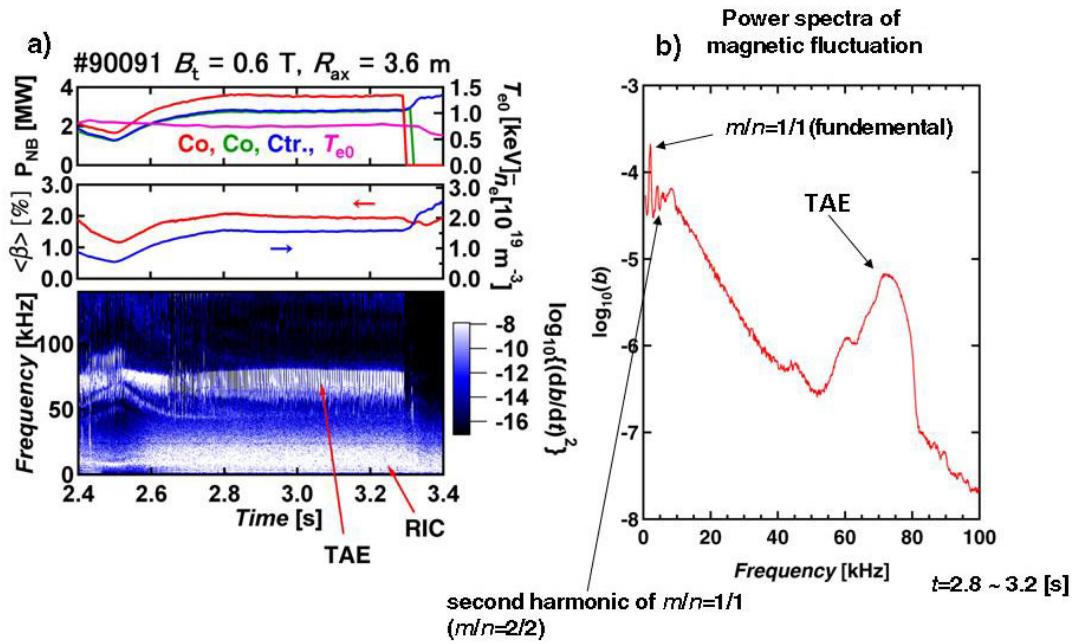
Fig. 3 a) Time evolutions of NBI absorbed powers, T_{e0}, the bulk plasma beta $\langle\beta\rangle$, the line-averaged electron density $\langle n_e\rangle$ and spectrogram of magnetic probe signal, where TAE ($m{\sim}1$, n=1) and RIC fluctuations (frequency <10 kHz) are identified. b) Power spectra of magnetic fluctuation. The dominant peak at 2 kHz frequency corresponds to RIC (m/n = 1/1). The smaller peak at $f{\sim}4$ kHz is the second harmonic of the RIC.
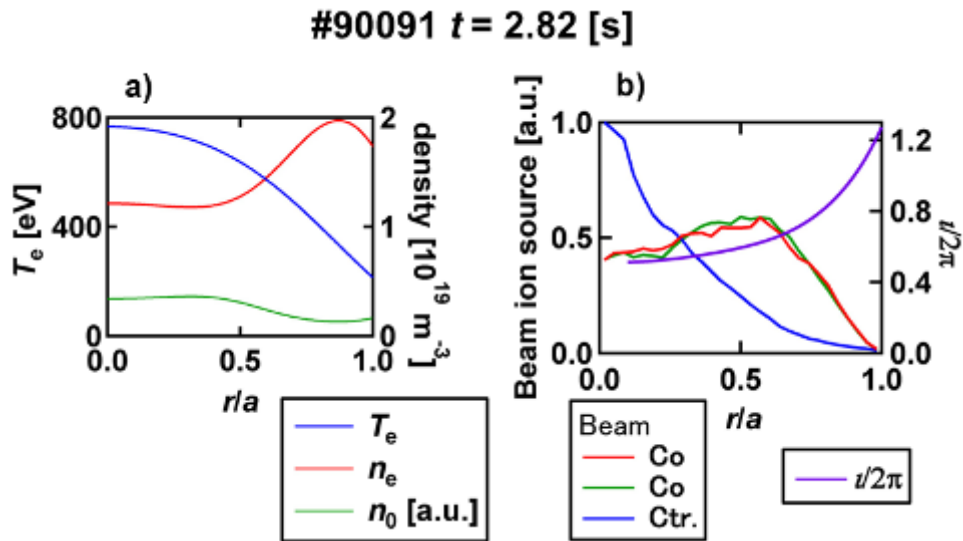
Fig. 4 a) Profiles of electron temperature, electron density, and neutral density at t = 2.82 s. Neutral density is inferred from the scaling of $1/n_e^2$. b) Radial profiles of deposited beam ions and the rotational transform $\iota/2\pi$ (inverse of safety factor) at t = 2.82 s, where the beam deposition profile is estimated using FIT code, and the $\iota/2\pi$ is calculated using VMEC2000 code.
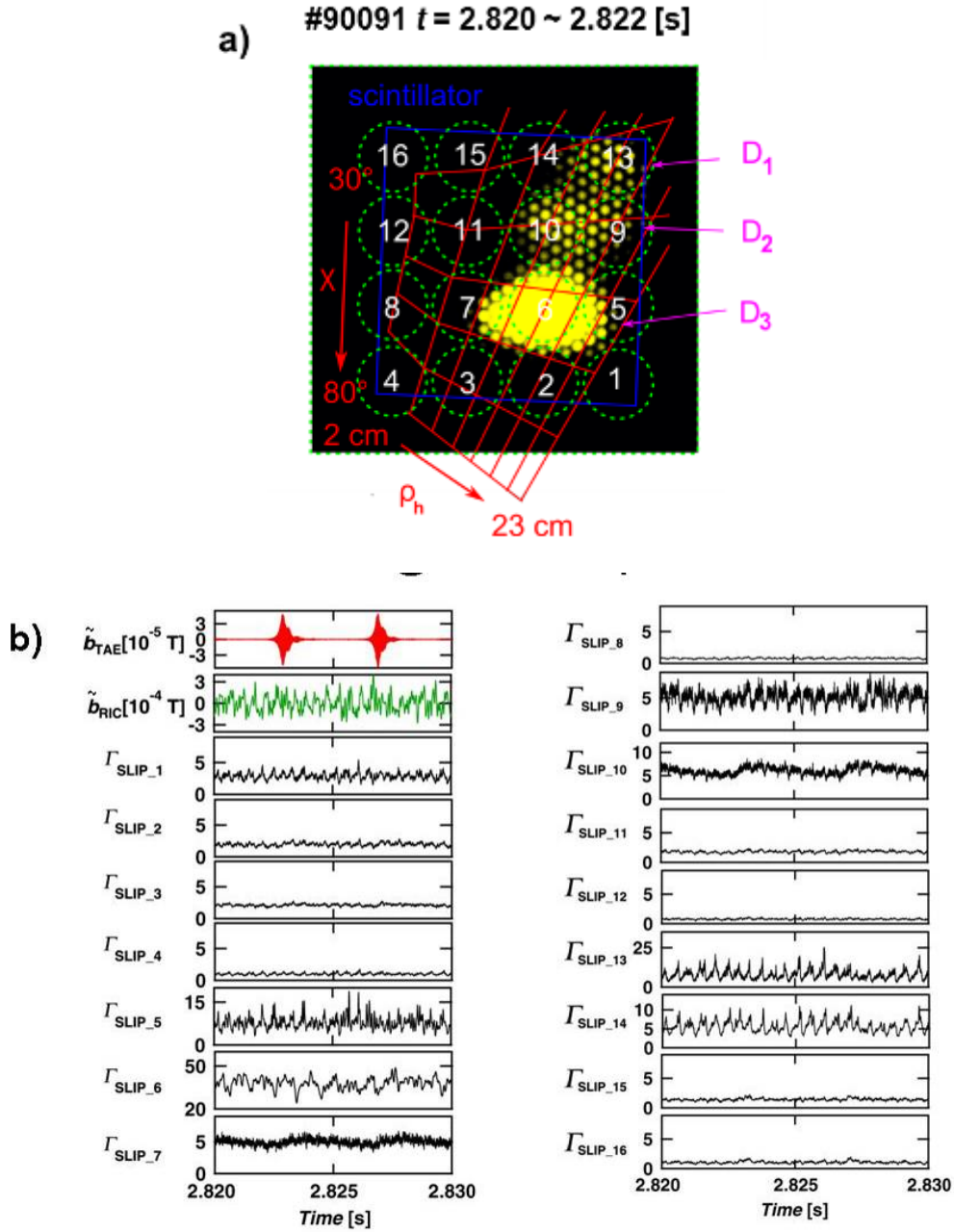
Fig. 5 a) Scintillation pattern captured with a CMOS camera. Three-dominant-loss domains (D_1, D_2 and D_3) are observed. The spot in the domain D_3 appears even if TAE/RIC is not excited. b) Time traces of magnetic fluctuations by TAE and RIC, and 16 SLIP signals. TAE-induced loss is

clearly observed in $\Gamma_{\text{SLIP\_7}}$, $\Gamma_{\text{SLIP\_9}}$ and $\Gamma_{\text{SLIP\_10}}$, of which detail is discussed in the subsection 3.2.

RIC-induced loss is clearly observed as frequent spikes in $\Gamma_{\text{SLIP\_5}}$, $\Gamma_{\text{SLIP\_6}}$, $\Gamma_{\text{SLIP\_13}}$ and $\Gamma_{\text{SLIP\_14}}$, of which detail is discussed in the subsection 3.3.
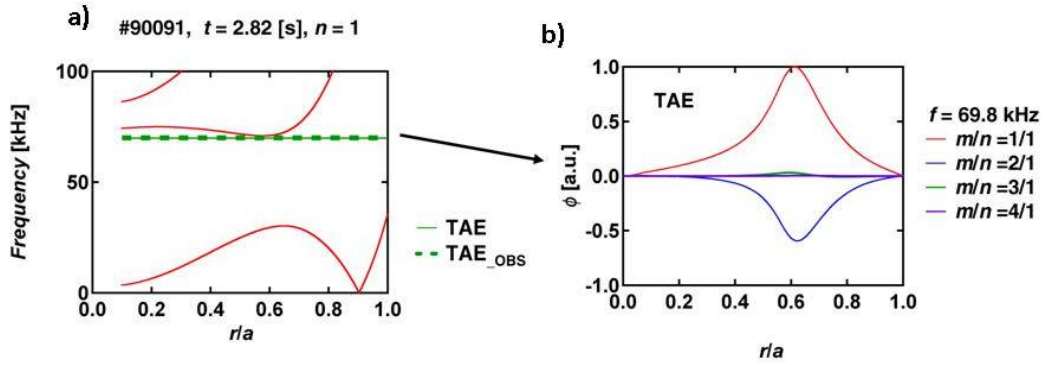
Fig. 6 a) Shear Alfvén spectra of n=1 calculated by the STELLGAP code, where $m = 0 \sim 10$

Fourier modes are included. In the calculation, profiles of n_e, and $\iota/2\pi$ shown in Fig4 are used.

The calculated and observed TAE frequencies are shown with thin and broken horizontal lines,

respectively.   b) Eigenfunction of the TAE mode calculated with AE3D.   This mode has the

odd radial parity.
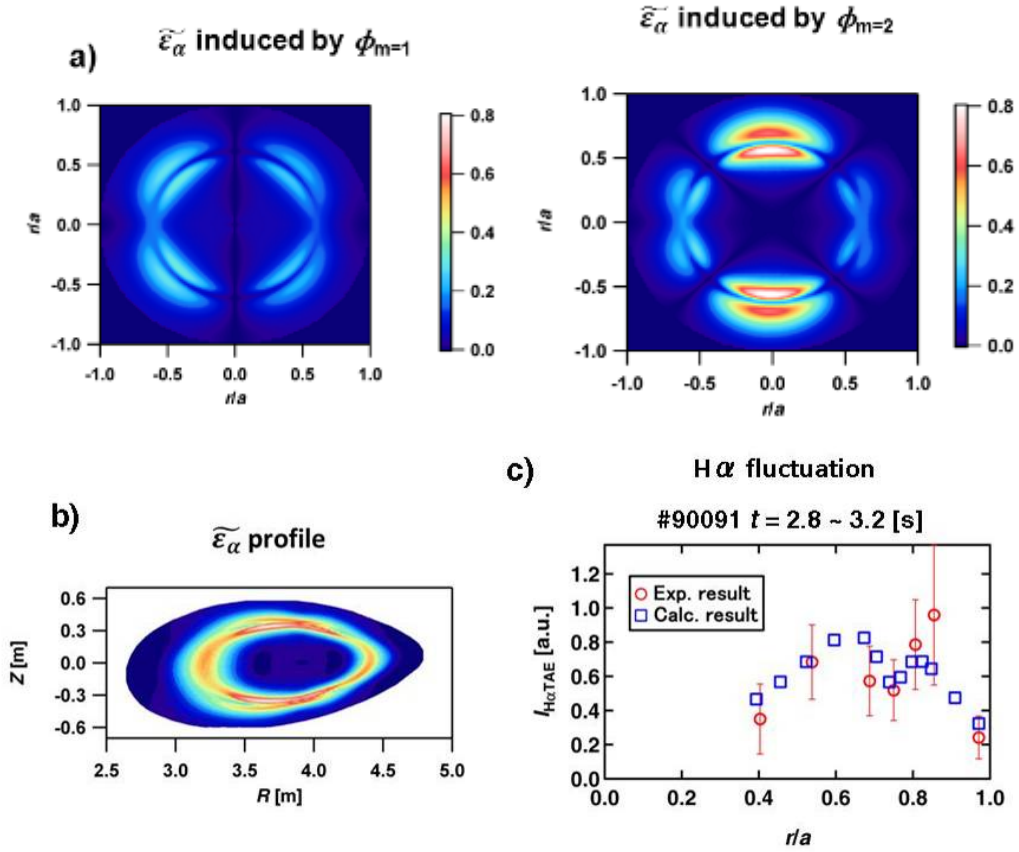
Fig. 7 a) Profiles of the local Hα (Hα emissivity) fluctuation induced by m=1 and m=2 Fourier

components of TAE eigenfunction calculated by AE3D where $n_0 \propto n_e^{-2}$ is assumed. b) Profile of

local Hα fluctuation induced by TAE in the cross section of the LHD plasma viewed by the

FHA diagnostic, where the mode pattern is uniform in the toroidal direction. The eigenfunction

of TAE is converted from that in the flux coordinate using in Fig. 7a to the real one based on

VMEC2000 calculation. c) The Hα fluctuation profile obtained experimentally with FHA (open

circles) and that calculated from the result shown in Fig.7 b that was calculated with AE3D code

(open squares). The mode pattern shown in Fig.7 b is rotated 10 times having 1000 steps for
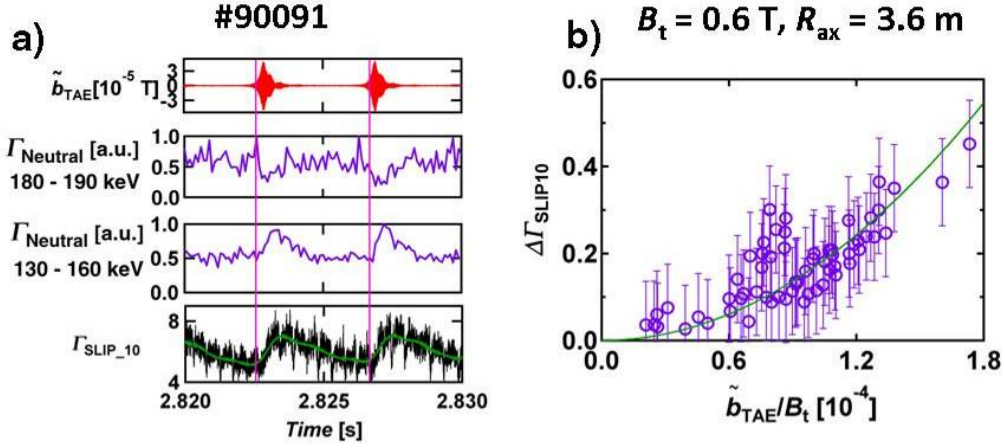
each rotation.

Fig. 8 a) Time traces of magnetic fluctuations of TAE, fast neutral flux measured with a tangential NPA ($\Gamma_{neutral}$) and Γ_{SLIP}. The fluxes $\Gamma_{neutral}$ in the range of E=130-160 keV and E=180-190keV are shown. In the trace of Γ_{SLIP_10} , the smoothed signal of Γ_{SLIP_10} is overlaid. The smoothing is done by numerical band pass filter to remove the modulations by RICs and also by moving average technique to suppress white noise. b) Dependence of the increment of the loss flux induced by TAE on magnetic fluctuation amplitude of TAE.
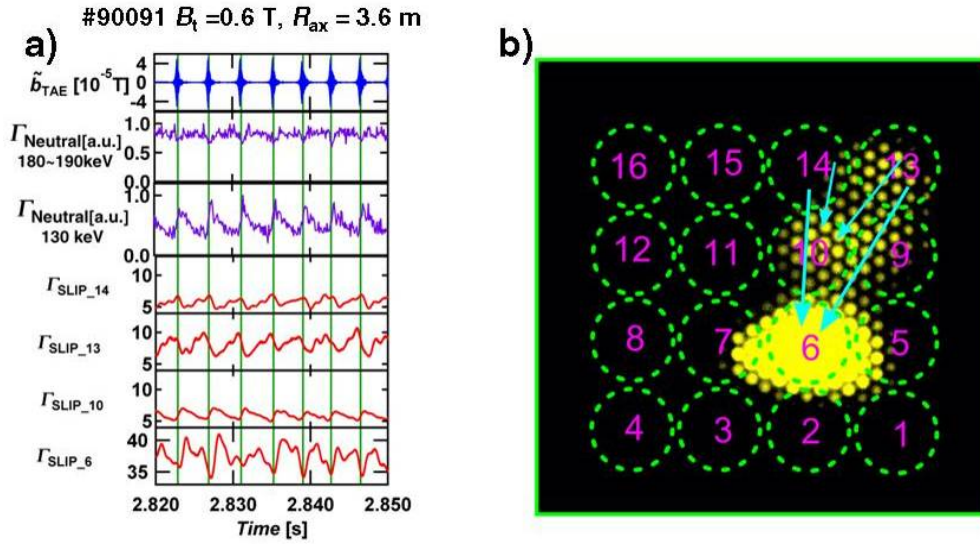
Fig. 9 a) Time traces of TAE magnetic fluctuations, Γ_{neutral}, and Γ_{SLIP} that RIC-induced modulations are removed. b) Scintillation pattern obtained by a CMOS camera in the phase of t=2.820s to 2.822s. Directions of the pitch angle scattering and the energy drop of energetic ions by TAE bursts are indicated with arrows.
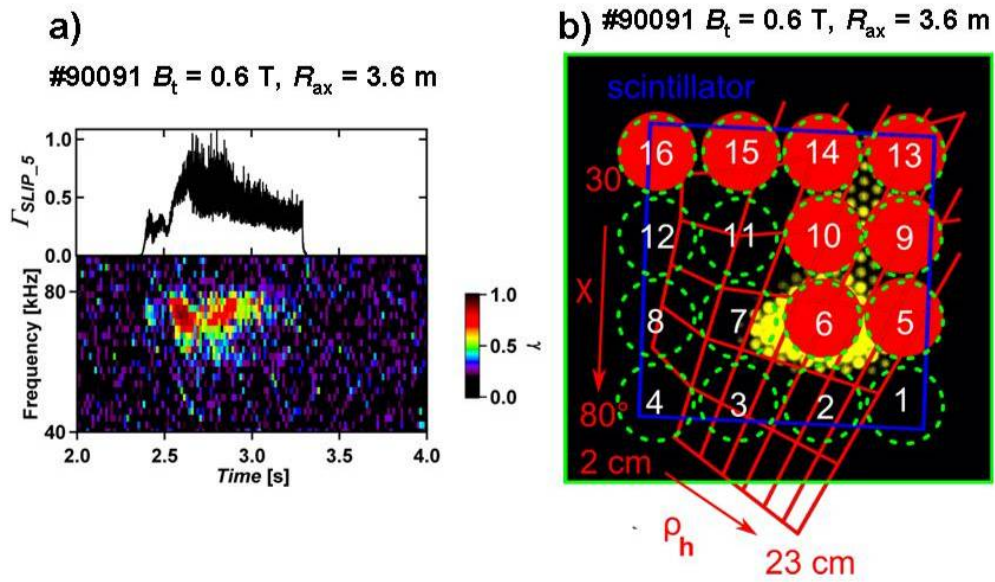
Fig. 10 a) Spectrogram of the coherence γ between $\Gamma_{\text{SLIP\_5}}$ and magnetic probe signal. Losses

correlated with TAE oscillations are observed with coherence analysis. b) Regions where high

correlation between magnetic probe signal and Γ_{SLIP} are observed (red circles). Especially, #15

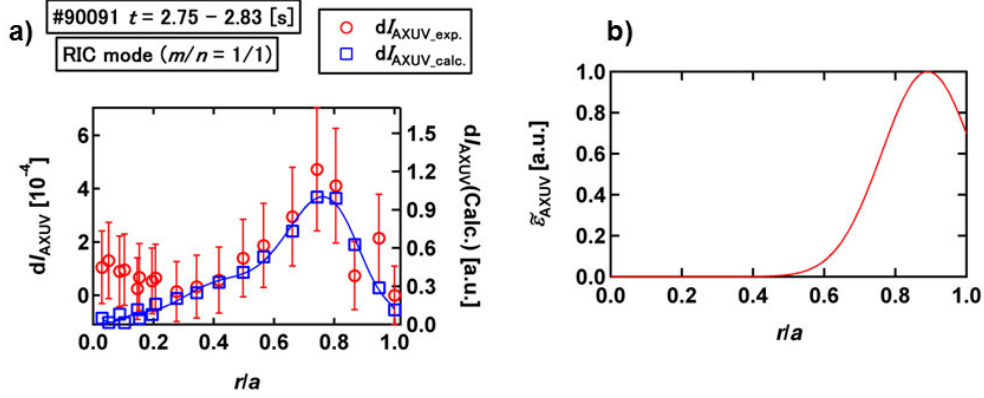and #5 regions have higher coherence.

Fig. 11 (a) Radial profiles of the amplitude of RIC fluctuations measured with AXUV array (open circles) and that from the calculation (open squares). Note that the signal dI_{AXUV} obtained by the AXUV array corresponds to the signal integrated along the sight lines shown in Fig.1d. The parameters x_o and w in the model profile of the local emissivity $\exp[\{(r/a-x_0)/w\}^2]$ was adjusted so that both profiles should have good agreement, where x_0 and w indicate the location of the rational surface and the island width. Here, $x_0=0.9$ and $w=0.2$ give the good agreement as shown in this figure. (b) Radial profile of local fluctuation of m/n=1/1 RIC derived from the AXUV fluctuation data in Fig.11a through the above model fitting. The x_0 agrees well with the predicted location of the $\iota/2\pi=1$ rational surface.
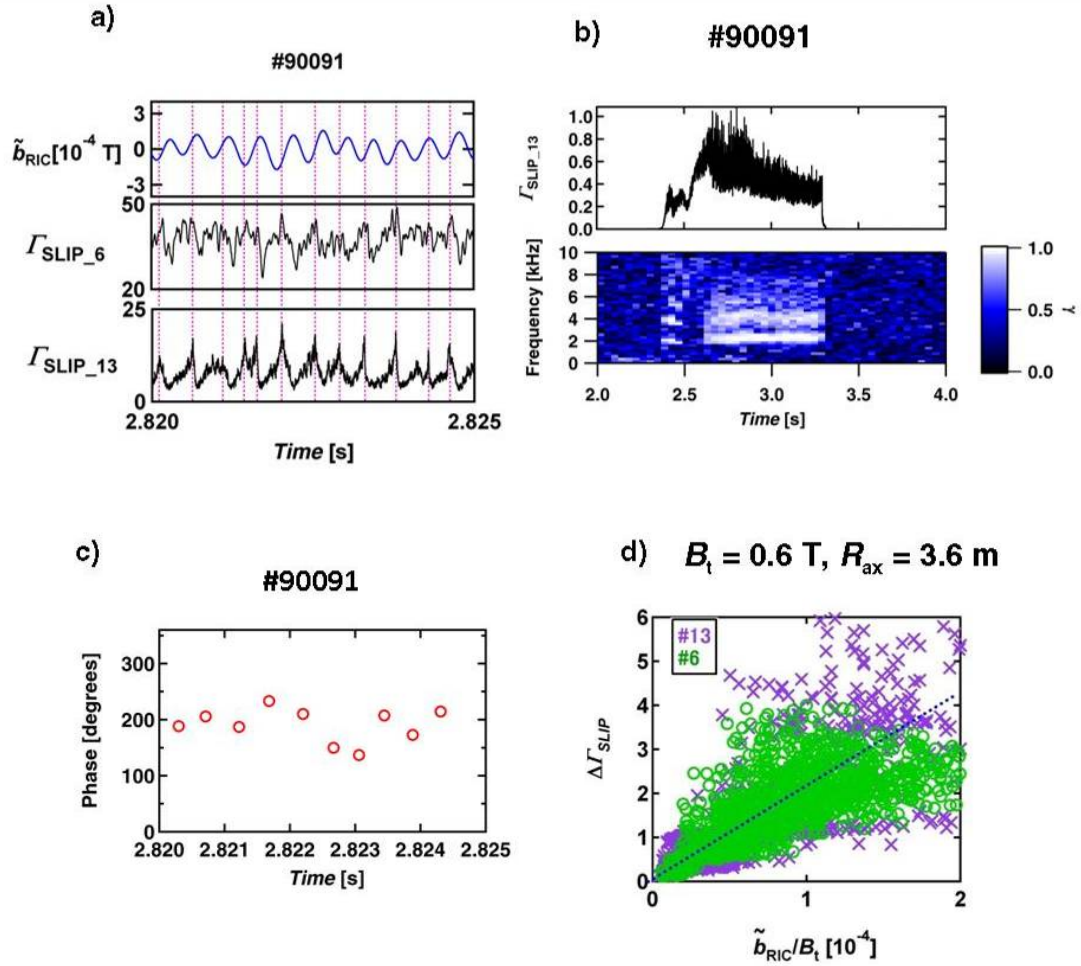
Fig. 12 a) Zoomed time evolution of RIC modes and Γ_{SLIP} signals. RIC magnetic fluctuations

are derived from MP signal by using numerical band-pass filter of 1.5 to 3 kHz. b) Spectrogram

of the coherence between Γ_{SLIP_13} and magnetic probe signal. The losses correlate with the

RIC-range oscillations (f = 2 kHz, 4 kHz). c) Time evolution of the phase difference between Γ_{SLIP13}

in the range of 1.5 kHz to 3.0 kHz and magnetic fluctuation of RIC mode. The average of the

phase is 185°±50°. d) Increment of losses due to RIC modes vs. the relative amplitude of RIC

magnetic fluctuations.